The Astrophysical Journal, 820:99 (13pp), 2016 April 1 doi:10.3847/0004-637X/820/2/99

DETECTION OF AN ATMOSPHERE AROUND THE SUPER-EARTH 55 CANCRI E

A. Tsiaras[1], M. Rocchetto[1], I. P. Waldmann[1], O. Venot[2], R. Varley[1], G. Morello[1], M. Damiano[1,3], G. Tinetti[1], E. J. Barton[1], S. N. Yurchenko[1], and J. Tennyson[1]
[1] Department of Physics & Astronomy, University College London, Gower Street, WC1E6BT London, UK; angelos.tsiaras.14@ucl.ac.uk
[2] Instituut voor Sterrenkunde, Katholieke Universiteit Leuven, Celestijnenlaan 200D, B-3001 Leuven, Belgium
[3] INAF–Osservatorio Astronomico di Palermo, Piazza del Parlamento 1, I-90134 Palermo, Italy
Received 2015 November 27; accepted 2016 February 5; published 2016 March 24

ABSTRACT

We report the analysis of two new spectroscopic observations in the near-infrared of the super-Earth 55 Cancri e, obtained with the WFC3 camera on board the *Hubble Space Telescope*. 55 Cancri e orbits so close to its parent star that temperatures much higher than 2000 K are expected on its surface. Given the brightness of 55 Cancri, the observations were obtained in scanning mode, adopting a very long scanning length and a very high scanning speed. We use our specialized pipeline to take into account systematics introduced by these observational parameters when coupled with the geometrical distortions of the instrument. We measure the transit depth per wavelength channel with an average relative uncertainty of 22 ppm per visit and find modulations that depart from a straight line model with a 6σ confidence level. These results suggest that 55 Cancri e is surrounded by an atmosphere, which is probably hydrogen-rich. Our fully Bayesian spectral retrieval code, $\mathcal{T}$-REx, has identified HCN to be the most likely molecular candidate able to explain the features at 1.42 and 1.54 μm. While additional spectroscopic observations in a broader wavelength range in the infrared will be needed to confirm the HCN detection, we discuss here the implications of such a result. Our chemical model, developed with combustion specialists, indicates that relatively high mixing ratios of HCN may be caused by a high C/O ratio. This result suggests this super-Earth is a carbon-rich environment even more exotic than previously thought.

Key words: methods: data analysis – methods: statistical – planets and satellites: atmospheres – planets and satellites: individual (55 Cancri e) – techniques: spectroscopic

1. INTRODUCTION

Transiting exoplanets are an invaluable source of information as they enable the measurement of a large number of orbital and planetary parameters. Especially when observed at different wavelengths, the thermal properties and composition of the exoplanetary atmosphere can be revealed (e.g., Seager & Sasselov 2000; Brown 2001; Tinetti et al. 2007a).

Using the transit technique, many teams have discovered molecular features in the atmospheres of exoplanets, both from the ground (e.g., Redfield et al. 2008; Snellen et al. 2008, 2010, 2014; Bean et al. 2010, 2013; Swain et al. 2010; Waldmann et al. 2012) and from space (e.g., Charbonneau et al. 2002, 2005; Deming et al. 2005, 2011; Knutson et al. 2007, 2008; Tinetti et al. 2007b, 2010; Swain et al. 2008, 2009a, 2009b, 2013).

Super-Earths are an intriguing class of planets as they do not exist within our solar system. Even basic information about their density seems to suggest that there is a variety of cases (e.g., Sotin et al. 2007; Valencia et al. 2007, 2013; Grasset et al. 2009; Zeng & Sasselov 2014). According to *Kepler* and radial velocity statistics, super-Earths are the most abundant planets, especially around late-type stars (e.g., Mayor et al. 2011; Howard et al. 2012; Dressing & Charbonneau 2013; Fressin et al. 2013). The Wide Field Camera 3 (WFC3) on board the *Hubble Space Telescope* (*HST*), combined with the recently implemented spatial scanning technique, allows the spectroscopic observation of super-Earths, which is unprecedented. Published observations of two super-Earths, GJ 1214b and HD 97658b, do not show any evident transit depth modulation with wavelength (Knutson et al. 2014b; Kreidberg et al. 2014b), suggesting an atmosphere covered by thick clouds or made of molecular species much heavier than hydrogen.

At a distance of only 12 pc, 55 Cancri is an extremely interesting planetary system hosting five planets, all discovered via radial velocity measurements (Butler et al. 1997; Marcy et al. 2002; McArthur et al. 2004; Fischer et al. 2008). Among them, 55 Cancri e is an "exotic" example of a super-Earth as it orbits very close to the host star, and consequently the temperature on its surface is high, i.e., hotter than 2000 K. The initially reported values for its period and minimum mass were 2.808 days and 14.21 ± 2.91 $M_{\oplus}$, respectively (McArthur et al. 2004). However, Dawson & Fabrycky (2010) revised these values, reporting a period of 0.7365 days and a minimum mass of 8.3 ± 0.3 $M_{\oplus}$.

Transits from space of 55 Cancri e were observed with the *Spitzer Space Telescope* (Demory et al. 2011) and *MOST* space telescope (Winn et al. 2011), confirming its small size ($\sim 2\,R_{\oplus}$). The eclipse depth of 131 ± 28 ppm observed by Demory et al. (2012) with *Spitzer*/IRAC at 4.5 μm converts to a brightness temperature of 2360 ± 300 K. Also, repeated eclipse observations suggested a variability of the thermal emission from the dayside of the planet over time (Demory et al. 2016). Table 1 summarizes the most recent parameters for 55 Cancri e. Given these parameters, Zeng & Sasselov (2014) have modeled the plausible structure of the interior and Hu & Seager (2014) have modeled the possible atmospheric compositions. These authors, together with others (e.g., Stevenson 2013; Forget & Leconte 2014), acknowledge that a gaseous envelope made of H_2 and He might have been retained from the protoplanetary disk.

In this work we analyze recent observations of the transit of 55 Cancri e obtained with the WFC3 camera on board the *Hubble Space Telescope*. Since the host star is very bright, these observations were obtained using spatial scans. This

Table 1
Observationally Determined Parameters of 55 Cancri e

Stellar parameters	
[Fe/H] (dex)[a]	0.31 ± 0.04
$T_{\rm eff}$ (K) [b]	5196 ± 24
M_* ($M_\odot$) [b]	0.905 ± 0.015
R_* ($R_\odot$) [b]	0.943 ± 0.010
$\log(g_*)$ (cgs)[b]	4.45 ± 0.001
Planetary parameters	
$T_{\rm eq}$ (K) [c]	1950^{+260}_{-190}
$M_{\rm p}$ ($M_\oplus$) [d]	8.09 ± 0.26
$R_{\rm p}$ ($R_\oplus$) [e]	$1.990^{+0.084}_{-0.080}$
a (AU)[e]	$0.01545^{+0.00025}_{-0.00024}$
Transit parameters	
T_0 (BJD) [e]	$2455962.0697^{+0.0017}_{-0.0018}$
Period (days)[e]	$0.7365417^{+0.0000025}_{-0.0000028}$
Rp/R_* [e]	$0.01936^{+0.00079}_{-0.00075}$
a/R_* [e]	$3.523^{+0.042}_{-0.040}$
i (deg)[e]	$85.4^{+2.8}_{-2.1}$

Notes.
[a] Valenti & Fischer (2005).
[b] von Braun et al. (2011).
[c] Crossfield (2012).
[d] Nelson et al. (2014).
[e] Dragomir et al. (2014).

technique allows the telescope to slew during the exposure to avoid saturation of the detector and has already been successfully used to provide an increasing number of exoplanetary spectra (e.g., Deming et al. 2013; Crouzet et al. 2014; Fraine et al. 2014; Knutson et al. 2014a, 2014b; Kreidberg et al. 2014a, 2014b, 2015; McCullough et al. 2014; Stevenson et al. 2014).

The scan rate used for the observations of 55 Cancri e ($4\farcs8\ {\rm s}^{-1}$) results in a very long scan of approximately 350 pixels. Typical scan lengths in currently published data sets vary between only 20 (XO1b—scan rate of $0\farcs05\ {\rm s}^{-1}$, Deming et al. 2013) and 170 pixels (HD 97658b—scan rate of $1\farcs4\ {\rm s}^{-1}$, Knutson et al. 2014b). This configuration can generate position-dependent systematics which need to be carefully removed. Our WFC3 scanning-mode dedicated pipeline (Tsiaras et al. 2015) was created to process such challenging data sets and it is able to correct the effects of geometric distortions. It can therefore provide a uniform analysis of different kinds of spatially scanned observations (Section 2.2). Finally, we use a range of techniques to correct for the time-dependent instrumental systematics known as "ramps" (Section 2.4), and calculate the wavelength-dependent transit depth.

The interpretation of the observed spectrum is carried out using our Bayesian spectral retrieval framework, $\mathcal{T}$-REx, described in Waldmann et al. (2015a, 2015b). In particular, we use the WFC3 data to constrain key atmospheric parameters such as the pressure at the surface, the atmospheric temperature, the main atmospheric component, and the abundance of trace gases. We also explore the possible correlations between said parameters. To check the consistency of the solution retrieved and to connect it to possible formation and evolution scenarios, we run in parallel an ab initio chemical model developed by Venot et al. (2012) to study hot exoplanets' atmospheres. This model allows us to explore the impact of different elemental compositions—in particular, the hydrogen fraction and the C/O ratio—on the molecular composition of the atmosphere.

2. DATA ANALYSIS

2.1. Observations

We downloaded the publicly available spectroscopic images of the transiting exoplanet 55 Cancri e (ID: 13665, PI: Björn Benneke) from the MAST Archive. The data set, obtained with the G141 grism, contains two visits of four *HST* orbits each. Each exposure is the result of three up-the-ramp samples with a size of 522×522 pixels in the SPARS10 mode, resulting in a total exposure time of 8.774724 s, a maximum signal level of 6.7×10^4 electrons per pixel, and a total scanning length of approximately 350 pixels. Both scanning directions were used for these observations, and in the text we will refer to them as forward (increasing row number) and reverse (decreasing row number) scans. In addition, the data set contains, for calibration purposes, a non-dispersed (direct) image of the target with the F132N filter.

The configuration of this particular data set allows us to fully capitalize on our WFC3 scanning-mode pipeline, as the long scanning length and the high scanning speed intensify the effects of the geometrical distortions, as discussed in Tsiaras et al. (2015). In addition, we can study the coupling between the scanning speed and the reading process which are critical elements in fast scanning observations (Section 2.3).

2.2. Extracting the Spectro-photometric Light Curves

In this section, we summarize the steps to extract the spectro-photometric light curves from the spatially scanned spectra. We refer the reader to Tsiaras et al. (2015) for a detailed discussion of our pipeline, which was conceived to reduce spatially scanned spectra.

The first step is the standard reduction of the raw scientific frames: bias drifts correction, zero read subtraction, nonlinearity correction, dark current subtraction, gain variations calibration, sky background subtraction, and finally bad pixel and cosmic-ray correction.

The next, fundamental, step is to calibrate the position of the frames, as this is required for wavelength calibration. In scanning-mode observations, position shifts are common. We measure the horizontal shifts by comparing the normalized sum across the columns of each frame to the first frame of the first visit. The forward and reverse scans are compared to the first forward or reverse scanned spectrum, respectively. This separation is necessary because the frames resulting from the two different scanning directions have slightly different positions on the detector and, consequently, slightly different structure, which could bias our measurement. For the vertical shifts, we make use of the first non-destructive read of each exposure. We fit an extended Gaussian function to each column profile because, due to the very fast scanning, even these spectra are elongated. Finally, we fit the central values of these extended Gaussians as a linear function of the column number, which indicates any possible vertical shifts. Again, we keep forward and reverse scans separated as their initial scanning positions are close to the two vertically opposite edges of the frame.

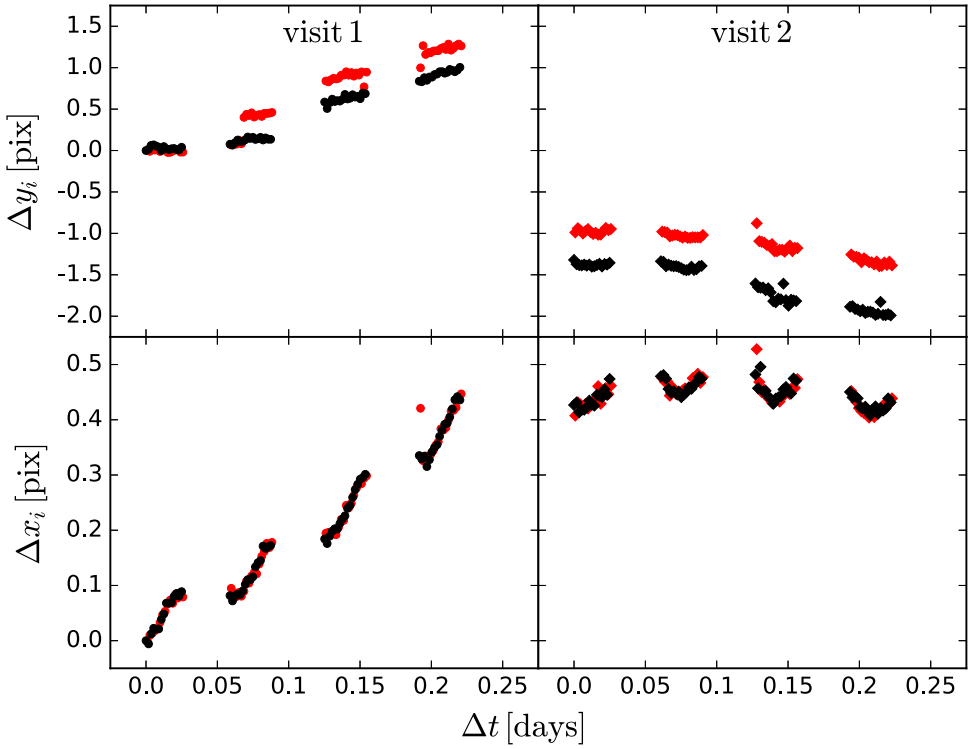

Figure 1. Vertical (top) and horizontal (bottom) shift for each frame of the two visits. The forward scans (black) are always compared to the first forward scan and the reverse scans (red) to the first reverse scan of the first visit.

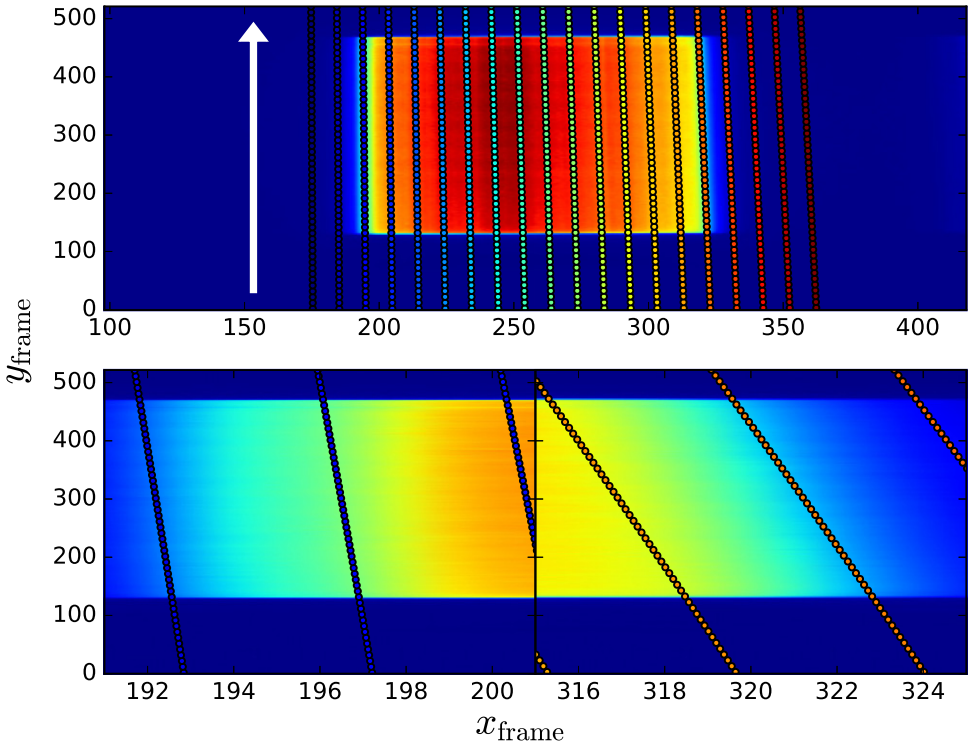

Figure 2. Top: wavelength-dependent photon trajectories (colored points) and the trajectory of the relative direct image (white arrow). Bottom: left and right edges of the spectrum where we can see the large difference between the position of photons with the same wavelength at the bottom and the top of the frame.

In the first visit, we find that the vertical shifts have an amplitude three times larger than the horizontal ones, while in the second visit they are five times larger (Figure 1). The behavior of the 55 Cancri e data set is not commonly observed and a plausible explanation is the high scanning speed used.

We then proceed to wavelength calibration. Based on the direct image included in the data set, the calibration coefficients

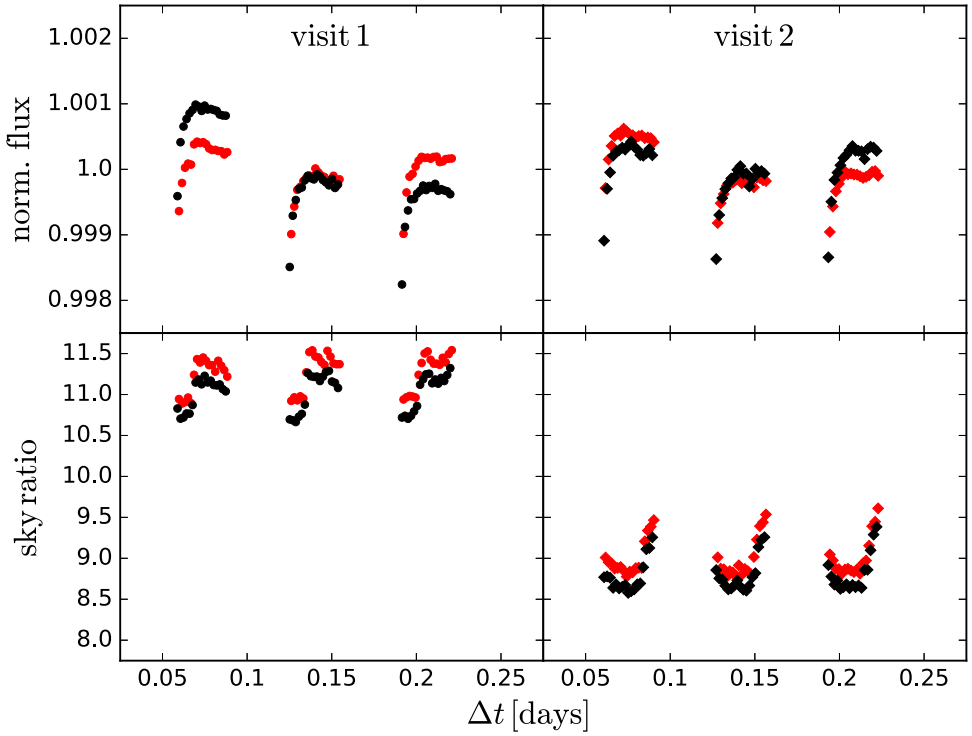

Figure 3. Top: raw white light curve for the forward (black) and reverse (red) scans, excluding the first orbit from each visit and normalized by the mean of each scanning direction for clarity. Bottom: sky background relative to the master sky frame for the two scanning directions in each visit.

provided by Kuntschner et al. (2009), and the measured horizontal shifts, we calculate the wavelength-dependent photon trajectories for each frame. The wavelength-dependent photon trajectories indicate the position of the photons at each wavelength on the detector during the scan.

As we can see in Figure 2, the position of the photons at a particular wavelength is shifted toward the left part of the detector as the scan processes. This behavior is caused by dispersion variations that our approach accurately takes into account. The effect on a single spatially scanned spectrum is that a pixel at the bottom of a given column is probing a different part of the stellar spectrum compared to a pixel at the top of the same column. For a column at $\sim$1.2 μm, the wavelength difference between the lower and the upper edge of the spatially scanned spectrum is 62 Å, 33% of the total bin size of 185 Å. The effect is stronger at longer wavelengths ($\sim$1.6 μm) where the difference is 140 Å, 57% of the total bin size of 230 Å. Given that the wavelength range inside one pixel is about 46 Å, in the first case the shift corresponds to 1.3 pixels, while in the second case to 3 pixels. We plan to further investigate how this bias propagates to the final planetary spectrum by using our WFC3 simulator, *Wayne* (Varley & Tsiaras 2015), in a future work.

The photometric apertures are delimited by the wavelength-dependent photon trajectories of a selected binning grid and, as a result, they are of quadrangular shape. We take into account fractional pixels by using a second-order, two-dimensional (2D) polynomial distribution of the flux (based on the values of the surrounding pixels) and calculating the integral of this function inside the photometric aperture. By applying this process to all of the frames, we extract the white (Figure 3) and spectral light curves.

2.3. Up-stream/Down-stream Effect: Exposure Time Variations Due to Vertical Position Shifts

Reading the IR detector of the WFC3 camera takes about 2.93 s in total and, as a result, while the exposure time is the same for all of the pixels, they are not all exposed simultaneously. The first and last rows of the detector are the first to be read, and then the process continues to the inner rows until the vertical mid-point is reached. The reading direction is, therefore, different for the two upper and the two lower quadrants, as the first are read downwards and the second upwards.

This process does not affect the staring-mode frames because the position of the spectrum is always the same. However, when the spatial scanning technique is used, there is a coupling between the scanning and reading directions, referred to as the down-stream/up-stream configuration, depending on whether the reading and scanning directions are the same/opposite. As a result, a down-stream configuration has a longer effective exposure time (McCullough & MacKenty 2012), which allows a longer total length for the scan and a higher total flux compared to an up-stream configuration.

Figure 3 clearly shows that the white light curves of the two different scanning directions have different long-term slopes. In particular, the reverse scans have an upward trend relative to the forward scans in the first visit, and a downward trend in the second visit. These trends are correlated with the vertical position shifts (Figure 1). Indeed, we find that the total length of the scans, i.e., the effective exposure time and therefore the total flux, changes with the vertical position shifts in a different way for the two scanning directions (Figure 4).

In cases where the spectrum trace crosses the mid-point line, the scanning/reading configuration is down-stream at the beginning of the scanning process and up-stream at the end of

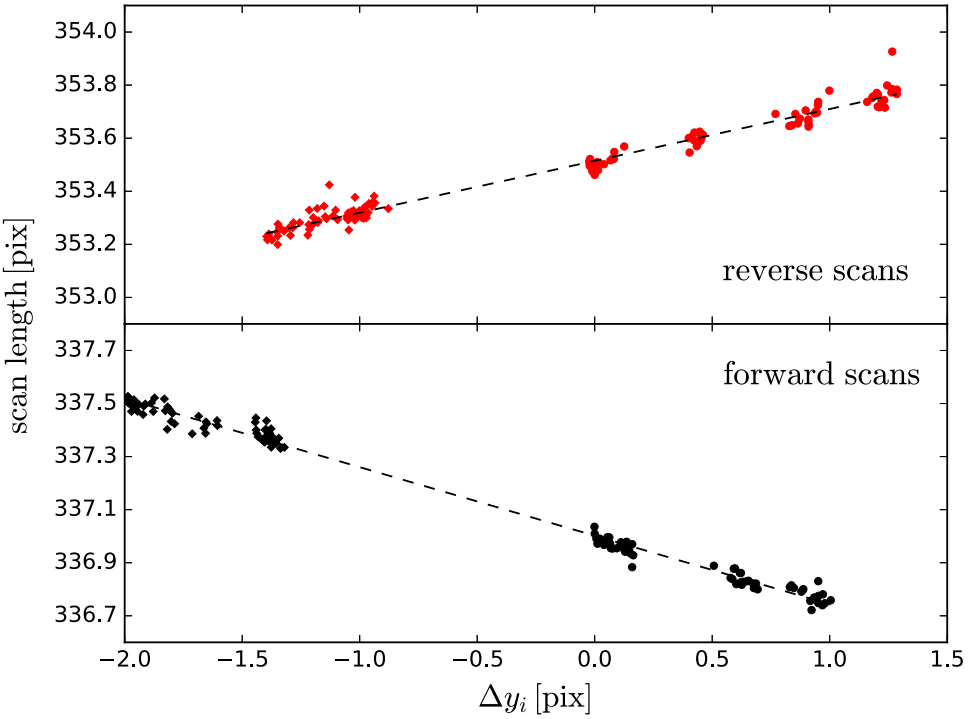

Figure 4. Scanning length variations with vertical position shifts for the two scanning directions in each visit (visit 1—circles, visit 2—diamonds) and fitted models. The shifts are calculated with respect to the first frame of the first visit for each scanning direction.

it. We believe that this effect could cause a dependency between the vertical position of the spectrum on the detector and the effective exposure time. For this data set, the flux variation is about 0.7×10^{-3} for a vertical shift of one pixel.

We correct for this effect using the linear behavior of the scanning length with the vertical position shifts (Figure 4) and rescaling each data point to the first of each scanning direction. Figure 5 plots both scanning directions, which are fitted together with the same model, proving the consistency between them. Note that there is still a small, constant offset between them, and so we have to fit for two different normalization factors.

2.4. Fitting the White and the Spectral Light Curves

The WFC3 infrared detector introduces time-dependent systematics, known as "ramps," both in staring mode (Berta et al. 2012; Swain et al. 2013; Wilkins et al. 2014) and scanning mode (Deming et al. 2013; Knutson et al. 2014a; Kreidberg et al. 2014b; Tsiaras et al. 2015) observations. The effect of these systematics is stronger with increasing flux and, since 55 Cancri is a very bright source, the presence of "ramps" is expected (Figure 3). We correct these systematics using an approach similar to that of Kreidberg et al. (2014b). We adopt an instrumental systematics function:

$$R(t) = (1 - r_a(t - t_v))(1 - r_{b1}e^{-r_{b2}(t-t_o)}) \qquad (, 1)$$

where t is the mid-time of each exposure, t_v is the time when the visit starts, t_o is the time when the orbit in which the frame belongs starts, r_a is the slop of the linear long-term "ramp," and (r_{b1}, r_{b2}) are the coefficients of the exponential short-term "ramp."

We use our transit light-curve model, which returns the relative flux, $F(t)$, as a function of time, given the limb darkening coefficients, a_n, the R_p/R_* ratio, and all of the orbital parameters (T_0, P, i, a/R_*, e, ω). The model is based on the nonlinear limb darkening law (Claret 2000) for the host star:

$$I(a_n, r) = 1 - \sum_{n=1}^{n=4} a_n(1 - (1 - r^2)^{n/4}). \qquad (2)$$

We derive the limb darkening coefficients from the ATLAS stellar model (Kurucz 1970; Howarth 2011) of a star similar to 55 Cancri (Table 1), using the sensitivity curve of the G141 grism between 1.125 and 1.65 μm (Table 2) to avoid its sharp edges. Since the ingress and egress of the transit are not included in the light curve (Figure 3), it is impossible to fit for the orbital parameters. We therefore fix the inclination, the a/R_* ratio, and the mid-transit point to the values listed in Table 1. We also assume a circular orbit.

The models of the systematics, $R(t)$, and the white transit light curve, $F_w(t)$, are both fitted to the white light curve following two different approaches: (a) fitting the transit model multiplied by the instrumental systematics and a normalization factor, $n_w^{scan}R(t)F_w(t)$, and (b) fitting the instrumental systematics, $R(t)$, on the out-of-transit points, correcting the light curve, and then fitting a normalized transit model, $n_w^{scan}F_w(t)$. The normalization factor, n_w^{scan}, changes to n_w^{for} when the scanning direction is upward and to n_w^{rev} when it is downward to account for the offset between them. Figure 5 shows only the case of simultaneous fitting, as both approaches give the same result for each visit. The final R_p/R_* ratio is well consistent between the two visits (Table 2). Figure 6 plots the correlations between the fitted parameters, showing no correlation between the R_p/R_* ratio and any of the parameters describing the systematics.

As we can see in Figure 3, the sky background is slightly different for the forward and reverse scans, indicating that the area from which the sky background level is estimated is

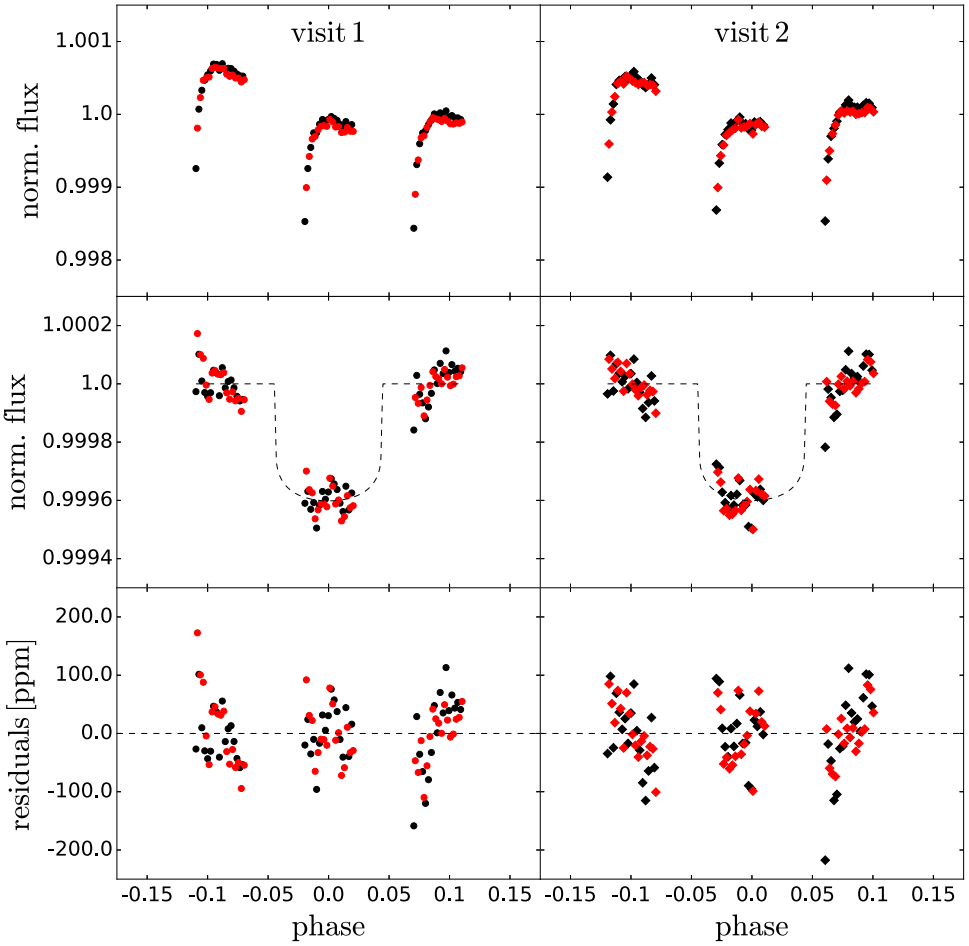

Figure 5. From top to bottom: (1) normalized raw light curve for the forward (black) and reverse (red) scans, (2) normalized light curve divided by the best-fit model for the systematics, compared to the fitted transit model, and (3) fitting residuals.

Table 2
White Light-curve Fitting Results

Limb Darkening Coefficients (1.125–1.650 μm)	
a_1	0.695623
a_2	−0.268246
a_3	0.357576
a_4	−0.171548
R_p/R_*	
visit 1	0.01894 ± 0.00023
visit 2	0.01892 ± 0.00023

contaminated by stellar flux. Since the area we are using is already at the left edge of the detector, this contamination is inevitable. To measure its effect on the final results, we repeat the whole process with an aperture that extends 10 pixels above and below the vertical edges of the spatially scanned spectrum (instead of the 20 used for the above results). We find a uniform shift of 3 ppm across the wavelength channels, while the uncertainty in the transit depth is, on average, 22 ppm for the relative spectral light curves. This result indicates that the relative structure of the spectrum is not affected, and the uncertainty in the R_p/R_* ratio includes this potential bias.

To calculate the wavelength-dependent transit depth, we use the spectral light curves divided by the white one. In this way, we minimize the effect of the systematics model not perfectly approximating the real systematics, as the residuals in Figure 5 do not follow a Gaussian distribution. The relative light curves appear to have an out-of-transit slope which we interpret as an effect caused either by the horizontal shifts (model 1) or by a wavelength-dependent, long-term "ramp" (model 2). In the first case, we fit for a factor which is linear with the horizontal shifts, as calculated in Section 2.2, while in the second case we fit for a factor which is linear with time. The models used for each of the above approaches are

$$\begin{aligned} &\text{model 1:} \quad n_\lambda^{\rm scan}(1 + \chi_\lambda \Delta x)(F_\lambda/F_{\rm w}) \\ &\text{model 2:} \quad n_\lambda^{\rm scan}(1 + \chi_\lambda t)(F_\lambda/F_{\rm w}) \end{aligned} \tag{3}$$

, where $n_\lambda^{\rm scan}$ is a normalization factor with the same behavior as in the white light curve, χ_λ is the linear factor in each case, $\Delta x = \Delta x(t)$ is the horizontal shifts, $F_{\rm w} = F_{\rm w}(t)$ is the white light-curve model, and is $F_\lambda = F_\lambda(t)$ the spectral light-curve model. Fitting the normalization factor per wavelength channel is necessary, as the offset between the scanning directions varies with wavelength. The orbital parameters used are those from Table 2 and the white R_p/R_* ratio is taken from the fitting above.

For each spectral light curve, we fit the above models twice: the first time, using the uncertainties provided by the reduction and extraction process, and the second using the standard

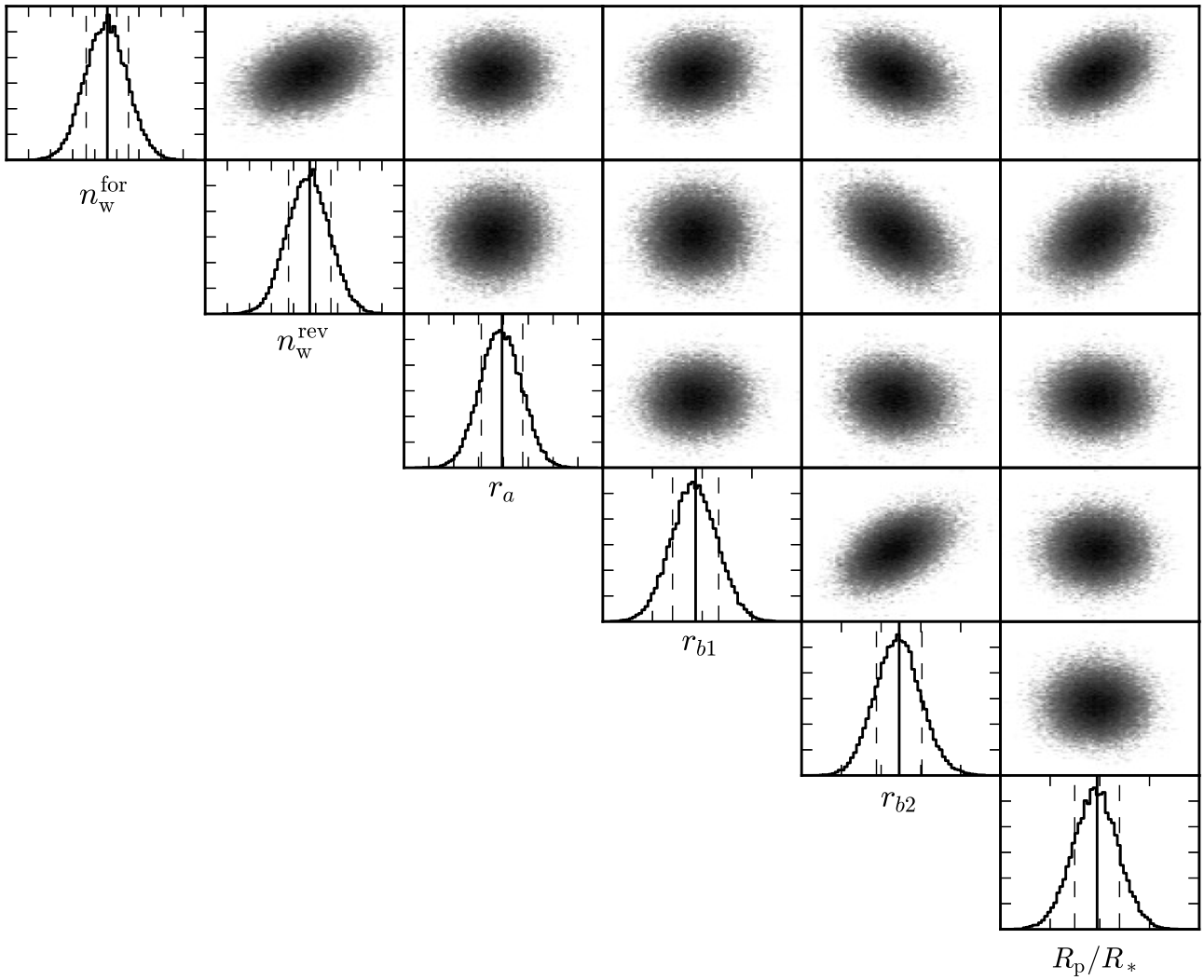

Figure 6. Correlations between the fitted systematics and transit parameters for the simultaneous fitting approach on the first visit data points. As we can see, apart from the expected correlation with the normalization factors, the $R_{\rm p}/R_*$ ratio is not correlated with any of the three parameters that describe the systematics.

deviation of the residuals of the first fit. The final uncertainty reported is the maximum of the two and it is between 5% and 20% above the photon noise limit. In this way, we take into account possible scatter in the data points that is in addition to the photon noise and the noise introduced by the instrument.

The wavelength bins are selected within the limits of the white light curve and with a constant resolution of $\lambda/\Delta\lambda = 65$, which is half of the resolving power of the G141 grism, to keep an approximately uniform signal-to-noise ratio (S/N). We calculate the limb darkening coefficients for each spectral light curve using the ATLAS model, the stellar parameters in Table 1, and the sensitivity curve of the G141 grism inside the boundaries of each wavelength bin.

2.5. Atmospheric Retrieval

In order to fit the WFC3 spectrum, we use $\mathcal{T}$-REx (Waldmann et al. 2015a, 2015b), a Bayesian spectral retrieval that fully maps the parameter space through a nested sampling algorithm. The transmission spectra are generated using cross sections based on the line lists from ExoMol (Barber et al. 2006; Yurchenko et al. 2011; Tennyson & Yurchenko 2012; Barton et al. 2013; Barber et al. 2014; Yurchenko & Tennyson 2014), HITRAN (Rothman et al. 2009, 2013), and HITEMP (Rothman et al. 2010). The atmosphere is parametrized assuming an isothermal profile with constant molecular abundances as a function of pressure. We include a wide range of molecules in the fit, including H_2O, HCN, NH_3, CH_4, CO_2, CO, NO, SiO, TiO, VO, H_2S, and C_2H_2. The fitted parameters are the mixing ratios of these molecules, the atmospheric mean molecular weight, the surface pressure, and the planetary radius.

We use uniform priors for the gas mixing ratios ranging from 1 to 10^{-8}. The mean molecular weight is coupled to the fitted composition in order to account for both the fitted trace gases and possible unseen absorbers with signatures outside the wavelength range probed here. The uniform prior assumed for the mean molecular weight ranges from 2 to 10 amu. Finally, we assume uniform priors for the surface radius, the surface pressure, and the mean atmospheric temperature in the range of 0.1–0.3 $R_{\rm Jup}$, 10–10^7 Pa, and 2100–2700 K, respectively. We do not include a separate parameterization for the cloud layer; the pressure at the surface could be the pressure at the top of a cloud deck.

2.6. Ab initio Chemical Simulations

In parallel to the spectral retrieval, we investigated the theoretical predictions for the chemical composition of an atmosphere enveloping 55 Cancri e. We assumed an atmosphere dominated by hydrogen and helium with a mean molecular weight of 2.3 amu. We used a thermal profile with a high-altitude atmospheric temperature of 1600 K. These parameters correspond to a scale height of 440 km, or 25 ppm, at the surface.

We used the same chemical scheme implemented in Venot et al. (2012) to produce vertical abundance profiles for 55 Cancri e, assuming a solar C/O ratio and a C/O ratio of 1.1. This chemical scheme can describe the kinetics of species with up to two carbon atoms. In Venot et al. (2015), it was shown that a more sophisticated chemical scheme including species with up to six carbon atoms produces comparable results, and that the simpler scheme can reliably model atmospheres with C/O ratios above 1. The scheme has been developed with combustion specialists and validated by experiments conducted in a wide range of temperatures (300–2500 K) and pressures (0.01–100 bar; e.g., Battin-Leclerc et al. 2006; Bounaceur et al. 2007, 2010; Anderlohr et al. 2010; Wang et al. 2010).

The stellar flux was calculated in the following manner. From 1 to 114 nm, we used the mean of the Sun spectra at maximum and minimum activity (Gueymard 2004), scaled to the radius and effective temperature of 55 Cancri. From 115 to 900 nm, we used the stellar flux of ε Eridani (HD 22049) from Segura et al. (2003), also scaled to the properties of 55 Cancri. ε Eridani is a K2V star ($T_{\rm eff} = 5084$ K and $R = 0.735\ R_{\rm Sun}$) quite close to 55 Cancri, which is a G8V star ($T_{\rm eff} = 5196$ K and $R = 0.943\ R_{\rm Sun}$), making ε Eridani a quite good proxy for 55 Cancri.

3. RESULTS

The results obtained with the two different fitting models described in Section 2.4 are plotted in Figure 7. In the first visit, the transit depths are consistent within 0.3σ and there is no preference between the two models, as fitting model 2 only improves the standard deviation of the residuals by 0.5% compared to model 1. In the second visit, the results are less consistent with each other (1.1σ) because the horizontal shifts have a very small amplitude and cannot explain the observed slope. In this case, fitting model 2 improves the standard deviation of the residuals by 10%, and therefore the final results that we report have been obtained with model 2. The calculated limb darkening coefficients (a_{1-4}) and the final measurements of the transit depths $(R_{\rm p}/R_*)^2$ as a function of wavelength are tabulated in Table 3. The transmission spectrum of 55 Cancri e and the best fits to it, obtained with $\mathcal{T}$-REx, are shown in Figure 8, while Figure 9 shows the posterior distributions of the fit to the spectrum using the model with HCN.

Regardless of the specific gas causing the absorption features on the right-hand side of the WFC3 spectrum, the mean molecular weight (μ) of the atmosphere peaks at about 4 amu, as shown by the posterior distribution in Figure 9. Higher values for the mean molecular weight would make the atmosphere more compact and the features weakened. The relatively strong absorption seen between 1.4 and 1.6 μm indicates that μ is relatively low, and that the atmosphere is likely dominated by a mixture of hydrogen and helium. Therefore, the spectral absorbing features seen in the spectrum should be attributed to trace gases, rather than the main atmospheric component. The posterior of the surface pressure peaks at 0.1 bar, but we note that the parameter is only loosely constrained by the data.

Among the molecules considered in the fit, we find that the best absorber that can fit the data is HCN. This species can adequately fit the absorption features seen at approximately 1.42 and 1.54 μm. All of the other absorbers show little or no contribution to the overall spectrum. Interestingly, we find no evidence of water vapor. Despite the result of the retrieval, we stress that with the current precision of the measurements and this restricted wavelength range, we cannot confirm the presence or absence of certain absorbers, in particular CO_2, C_2H_2, and CO.

We find that the posterior distribution of HCN tends to favor a scenario with a high absolute mixing ratio, but the acceptable values are broad, starting at 10^{-5}. We note the degeneracy between the HCN mixing ratio and the surface pressure: the lower the HCN abundance, the higher the surface pressure. Finally, we find that the temperature is very poorly constrained by this data. For our best-fit model, which includes HCN, the scale height of the atmosphere is 242 km, or 14 ppm (with $T = 2100$ K, $\mu = 3.2$ amu, $R_{\rm p} = 0.17\ R_{\rm Jup}$). Given this value, the amplitude of the spectral modulation of 70 ppm corresponds to 5 scale heights.

We also run other models to verify the validity of this result. We find that a straight line fit has a $\chi^2 = 89.4$, which, with 24 degrees of freedom, indicates that a straight line can be rejected with a 6σ confidence level. We also try to fit a model containing only a mixture of hydrogen and helium and no other trace gases. This model, which shows only the H_2–H_2 and H_2–He collision-induced absorption (dashed line in Figure 8), has a $\chi^2 = 39.6$.

As the nested sampling algorithm implemented in $\mathcal{T}$-REx allows the precise computation of the global evidence of each model, we can also perform model comparison in a Bayesian framework. Table 4 summarizes the global evidence and χ^2 values of the different models. We find that the straight line model has a log-evidence of 206.8, the model containing hydrogen and helium has $\log E = 226.2$, and the model containing HCN has $\log E = 228.8$. The Bayes factor B_m, defined as the ratio between the evidence of two different models, shows that we can confidently reject the straight line model. We find that the Bayes factors for the models with HCN or hydrogen and helium are 20 times larger compared to the straight line model, suggesting a very strong preference for the former two models according to the Jeffreys' scale. Finally, the Bayes factor for the model with HCN is 2.6 times larger compared to the model with hydrogen and helium, suggesting a moderate preference for the model with HCN.

Interestingly, we find that the spectrum obtained using the results of the ab initio model with a C/O greater than one is very close to the best fit found with $\mathcal{T}$-REx (see Figure 8). In this case, we obtain a χ^2 of 26.1. Figure 10 shows the vertical abundance profiles for the two cases with C/O ratio solar (top) and C/O = 1.1 (bottom). It can clearly be seen that the two scenarios are significantly different. For the solar C/O case, the dominant absorbing gases are CO and H_2O, with mixing ratios of $\approx 3 \times 10^{-4}$ and 4×10^{-4}, respectively. On the contrary, for C/O = 1.1, while CO still remains the dominant species at 10^{-3}, H_2O decreases to 10^{-7}–10^{-8}, and HCN and C_2H_2 increase to about 10^{-5}.

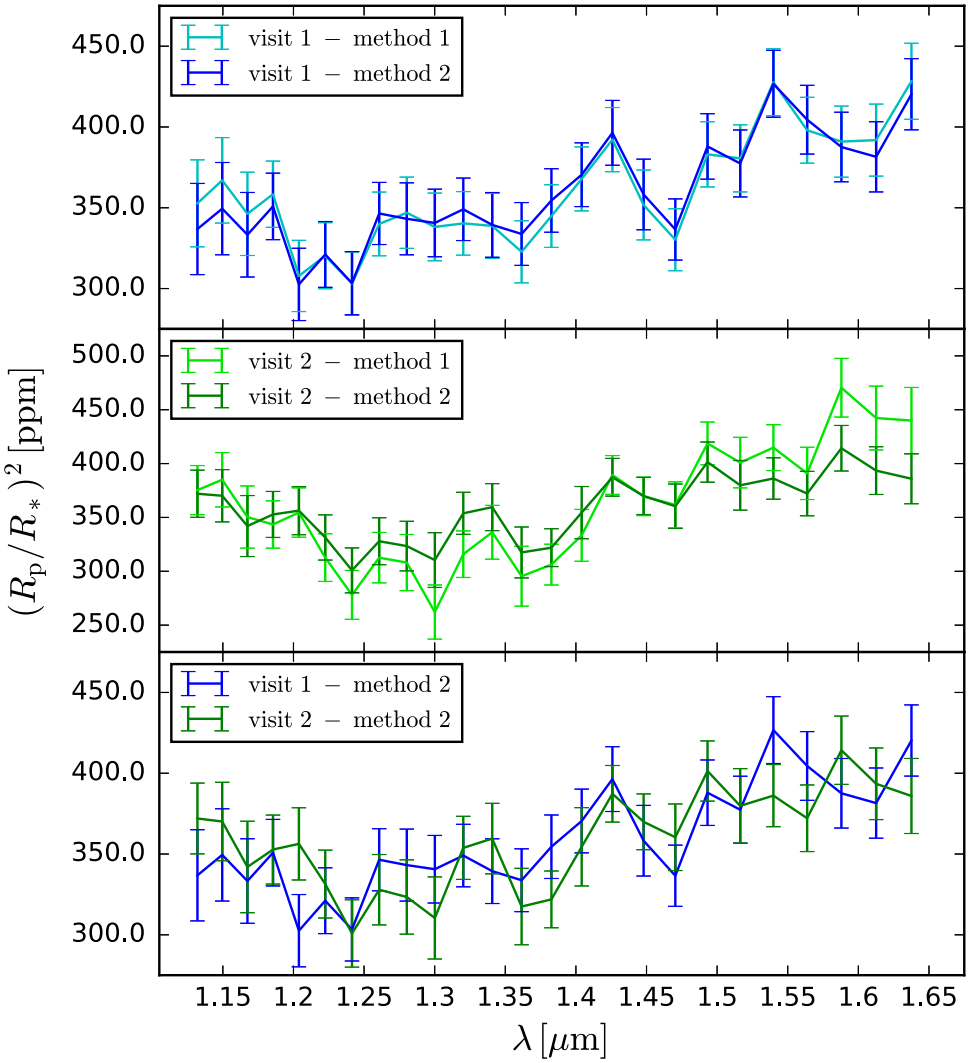

Figure 7. Results from fitting the spectral light curves. From top to bottom: (1) comparison of the two models for the first visit, (2) comparison of the two models for the second visit, and (3) comparison of model 2 for both visits.

The absolute abundance of HCN expected for a C/O = 1.1 scenario is roughly consistent with what we found in the retrieved spectrum, being at the end of the left tail of the posterior distribution of the fit (Figure 9). The transmission spectrum obtained using the abundances profiles for the C/O = 1.1 ratio is shown in Figure 8 (green line), and shows that it is roughly consistent with the retrieved spectrum. The dominant absorber in this wavelength range seen in this ab initio model is HCN, while other relatively strong absorbers, such as CO, C_2H_2, and CH_4, are all hidden below the HCN absorption.

4. DISCUSSION

4.1. Atmospheric Features in the Atmosphere of 55 Cancri e

The absorbing features seen in the spectrum of 55 Cancri e are indicative of the presence of an atmosphere. Our spectral retrieval shows that the atmosphere is likely dominated by a mixture of hydrogen and helium, and suggests that the features seen are mainly due to HCN. No signature of water vapor is found.

4.2. HCN as a Tracer of High C/O Ratio Atmospheres

If the features seen at 1.42 and 1.54 μm are due to hydrogen cyanide (HCN), then the implications for the chemistry of 55 Cancri e are considerable. Venot et al. (2015), using a new chemical scheme adapted to carbon-rich atmospheres, pointed out that the C/O ratio has a large influence on the C_2H_2 and HCN content in the exoplanet atmosphere, and that C_2H_2 and HCN can act as tracers of the C/O ratio. Indeed, in a large range of temperatures above 1000 K, at a transition threshold of about C/O = 0.9, the C_2H_2 and HCN abundances increase by several orders of magnitude, while the H_2O abundance decreases drastically, as sown in Figure 10.

We conclude that if the absorption feature is confirmed to be due to HCN, then the implications are that this atmosphere has a C/O ratio higher than solar. However, additional data in a broader spectral range are necessary to confirm this scenario. We also note that while there is a good line list available for the hot HCN/HNC system (Harris et al. 2002; Barber et al. 2014), there is no comprehensive line list available for hot C_2H_2; providing such a list is important for future studies of this interesting system.

Table 3
Limb Darkening Coefficients a_{1-4} and Transit Depth $(R_p/R_*)^2$ for the Wavelength Channels

$\lambda_1 - \lambda_2$ [μm]		a_1	a_2	a_3	a_4	$(R_p/R_*)^2$ (ppm)		
						Visit 1	Visit 2	W. Average
1.1233	1.1407	0.772891	−0.719847	0.973720	−0.395615	337 ± 28	372 ± 23	358 ± 18
1.1407	1.1584	0.748548	−0.643287	0.890964	−0.366607	349 ± 29	370 ± 24	361 ± 18
1.1584	1.1764	0.738983	−0.606810	0.847497	−0.353214	333 ± 26	342 ± 28	337 ± 19
1.1764	1.1946	0.729208	−0.572574	0.800655	−0.335301	351 ± 21	353 ± 22	352 ± 15
1.1946	1.2131	0.725726	−0.564131	0.785763	−0.330767	303 ± 22	357 ± 22	329 ± 16
1.2131	1.2319	0.697907	−0.466097	0.687658	−0.298018	321 ± 20	332 ± 21	326 ± 14
1.2319	1.2510	0.692692	−0.446746	0.662990	−0.289484	303 ± 20	301 ± 21	302 ± 14
1.2510	1.2704	0.685452	−0.409084	0.612133	−0.271088	346 ± 20	328 ± 22	338 ± 15
1.2704	1.2901	0.685892	−0.378366	0.574713	−0.270881	343 ± 22	324 ± 23	333 ± 16
1.2901	1.3101	0.673686	−0.354792	0.546395	−0.250464	341 ± 21	311 ± 25	328 ± 16
1.3101	1.3304	0.669421	−0.331802	0.512473	−0.238250	349 ± 20	354 ± 20	351 ± 14
1.3304	1.3511	0.660777	−0.276281	0.439988	−0.211147	339 ± 20	360 ± 22	348 ± 15
1.3511	1.3720	0.659749	−0.252857	0.401237	−0.196660	334 ± 20	318 ± 24	327 ± 15
1.3720	1.3933	0.652560	−0.189532	0.311675	−0.162120	354 ± 20	322 ± 20	338 ± 14
1.3933	1.4149	0.650933	−0.175302	0.300256	−0.163030	370 ± 20	355 ± 24	363 ± 15
1.4149	1.4368	0.650697	−0.189841	0.330447	−0.180237	396 ± 20	387 ± 19	391 ± 14
1.4368	1.4591	0.650529	−0.135161	0.234549	−0.139640	358 ± 22	370 ± 19	365 ± 14
1.4591	1.4817	0.639029	−0.076708	0.161044	−0.112436	337 ± 20	361 ± 21	348 ± 14
1.4817	1.5047	0.655337	−0.083499	0.125497	−0.091207	388 ± 20	402 ± 20	394 ± 14
1.5047	1.5280	0.660770	−0.025056	0.023486	−0.048336	377 ± 21	380 ± 23	378 ± 16
1.5280	1.5517	0.686804	−0.012316	−0.049479	−0.011120	427 ± 21	386 ± 20	405 ± 14
1.5517	1.5758	0.721349	−0.080742	−0.011227	−0.017553	404 ± 21	372 ± 21	388 ± 15
1.5758	1.6002	0.756804	−0.185811	0.070349	−0.038516	388 ± 22	414 ± 21	402 ± 15
1.6002	1.6250	0.801062	−0.222450	0.054906	−0.024391	382 ± 23	394 ± 22	388 ± 16
1.6250	1.6502	0.828396	−0.271626	0.075149	−0.025545	420 ± 23	386 ± 23	404 ± 16

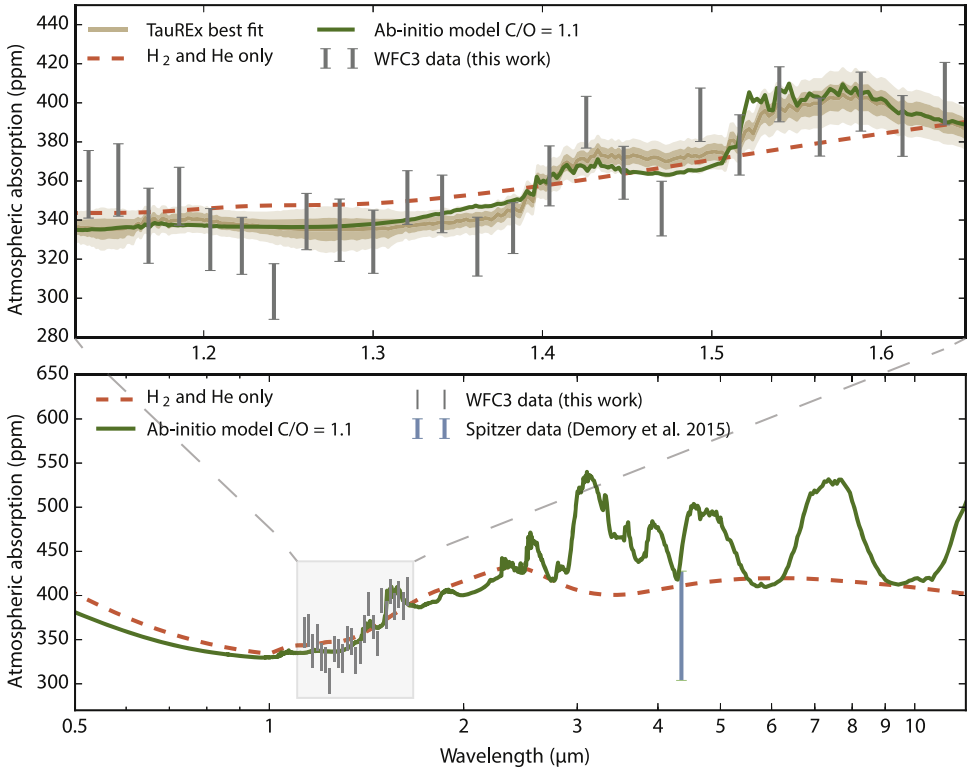

Figure 8. Top: infrared transmission spectrum of the hot super-Earth 55 Cancri e (gray error bars), best fit obtained with $\mathcal{T}$-REx (brown line), fitted model containing hydrogen and helium (dashed orange line), and an ab initio model with C/O = 1.1 (green line, see also Section 4.2). The shaded regions show the the 1 and 2σ confidence intervals in the the retrieved spectrum. Bottom: the same hydrogen/helium and ab initio models plotted in a broader wavelength range. As we can see, the two models can be better distinguished at longer wavelengths. The average transit depth of 55 Cancri e at 4.5 mu obtained with *Spitzer Space Telescope* (Demory et al. 2016) is also shown in light blue.

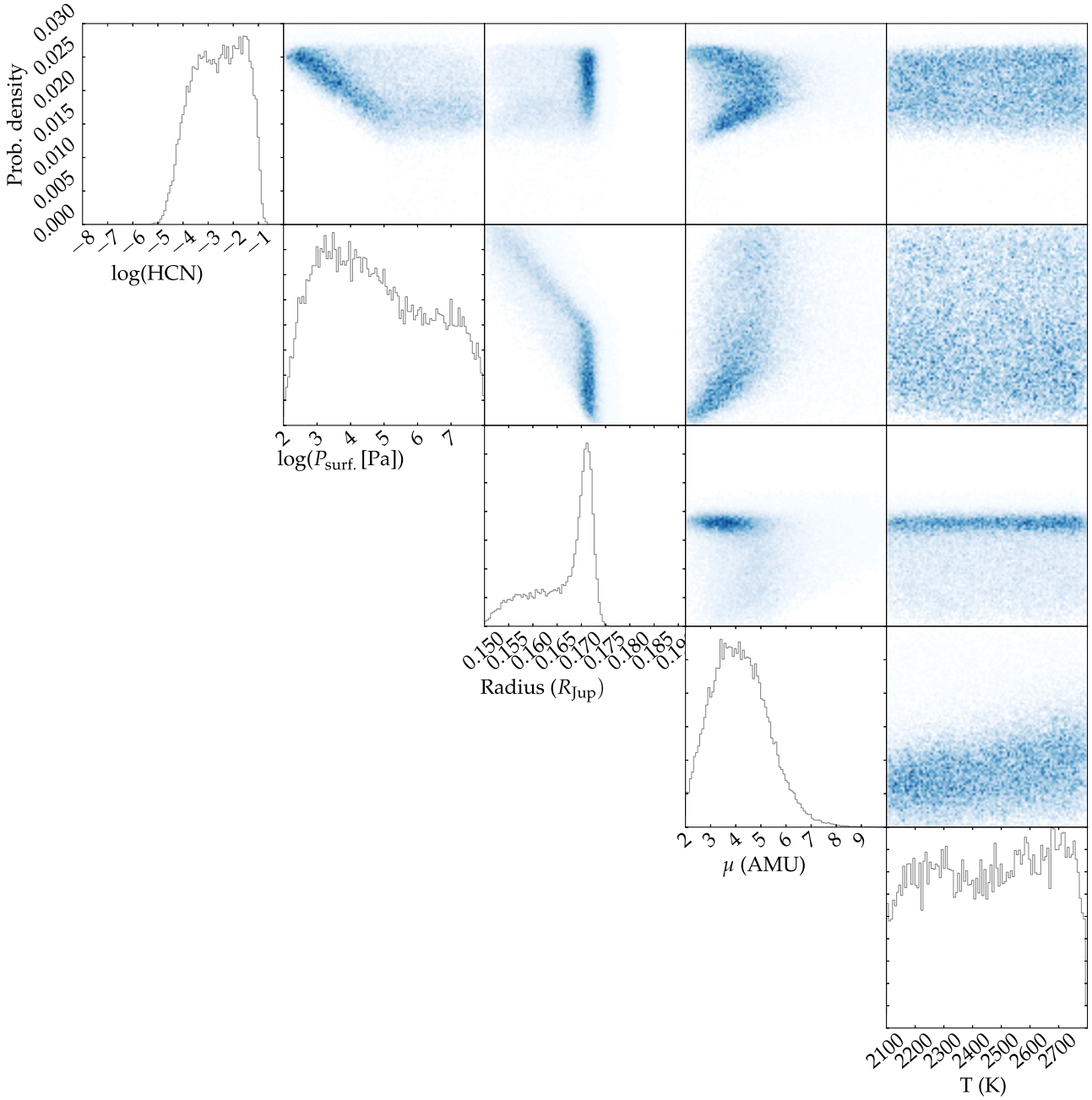

Figure 9. Posterior distributions of the retrieved atmospheric parameters and trace gases. Among all of the molecules considered in the fit, here we only show the posterior of HCN, as all the other molecules show little or no contribution to the spectrum.

Table 4
Log-evidence ($\log E$) and χ^2 Values for the Different Models Shown in Figure 8

Model	$\log E$	χ^2
Straight line	206.8	89.4
Helium and hydrogen only	226.2	39.6
Best fit (including HCN)	228.8	23.7
Ab initio model with C/O = 1.1	...	26.1

5. CONCLUSIONS

In this paper, we presented the first analysis of the two *HST*/WFC3 scanning-mode spectroscopic observations of the super-Earth 55 Cancri e.

In the case of very long scans, we have to take into account the geometric distortions (dispersion variations across the scanning direction and inclined spectrum) and the positional shifts (horizontal and vertical), as their effect on the structure of the spatially scanned spectrum becomes significant. Especially for fast scans, we found that the vertical shifts are as important as the horizontal ones because they are coupled with the reading process of the detector (up-stream/down-stream effect), causing exposure time variations. We also found that the time-dependent, long-term systematics appear to have a different behavior per wavelength channel.

The observed spectrum was analyzed with the $\mathcal{T}$-REx retrieval code. We identified a few important facts.

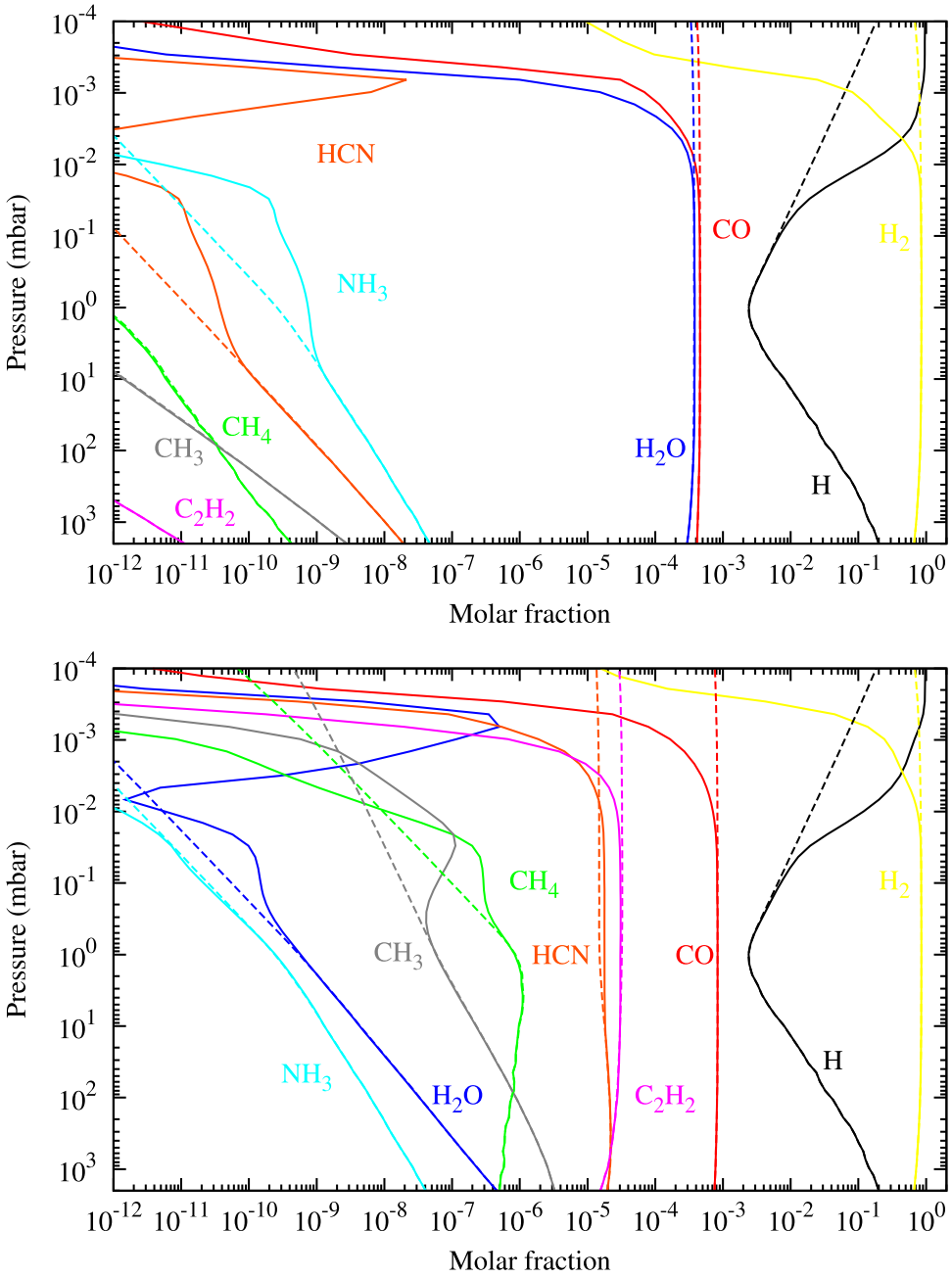

Figure 10. Vertical abundance profiles for the scenario with C/O solar (top) and C/O = 1.1 (bottom). The chemical compositions are calculated with the chemical scheme presented in Venot et al. (2012) and includes the effects of photochemistry. The chemical equilibrium is also represented (dashed lines).

1. The planet has an atmosphere, as the detected spectral modulations are 6σ away from a straight line model.
2. The atmosphere appears to be light-weight, suggesting that a significant amount of hydrogen and helium is retained from the protoplanetary disk.
3. There is no evidence of water vapor.
4. The spectral features at 1.42 and 1.54 μm can best be explained by HCN, with a possible additional contribution of other molecules, such as CO, CO_2, and C_2H_2.
5. This scenario is consistent with a carbon-rich atmosphere (e.g., C/O ratio = 1.1) dominated by carbon bearing species. The model for such an atmosphere was computed independently.

While our results have important implications for the study of 55 Cancri e and other super-Earths, further spectroscopic observations in a broader wavelength range in the infrared are needed to confirm our conclusions.

This work was supported by STFC (ST/K502406/1) and the ERC projects ExoLights (617119) and ExoMol (267219). O.V. acknowledges support from the KU Leuven IDO project IDO/10/2013 and from the FWO Postdoctoral Fellowship programme.

REFERENCES

Anderlohr, J., Pires da Cruz, A., Bounaceur, R., & Battin-Leclerc, F. 2010, CST, 182, 39

Barber, R. J., Strange, J. K., Hill, C., et al. 2014, MNRAS, 437, 1828
Barber, R. J., Tennyson, J., Harris, G. J., & Tolchenov, R. N. 2006, MNRAS, 368, 1087
Barton, E. J., Yurchenko, S. N., & Tennyson, J. 2013, MNRAS, 434, 1469
Battin-Leclerc, F., Bounaceur, R., Belmekki, N., & Glaude, P. 2006, Int. J. Chem. Kinet., 38, 284
Bean, J. L., Désert, J.-M., Seifahrt, A., et al. 2013, ApJ, 771, 108
Bean, J. L., Miller-Ricci Kempton, E., & Homeier, D. 2010, Natur, 468, 669
Berta, Z. K., Charbonneau, D., Désert, J.-M., et al. 2012, ApJ, 747, 35
Bounaceur, R., Glaude, P., Fournet, R., et al. 2007, Int. J. Veh. Des., 44, 124
Bounaceur, R., Herbinet, O., Fournet, R., et al. 2010, SAE, Tech. Pap. 2010-01-0546 (Warrendale, PA: SAE Int.)
Brown, T. M. 2001, ApJ, 553, 1006
Butler, R. P., Marcy, G. W., Williams, E., Hauser, H., & Shirts, P. 1997, ApJL, 474, L115
Charbonneau, D., Allen, L. E., Megeath, S. T., et al. 2005, ApJ, 626, 523
Charbonneau, D., Brown, T. M., Noyes, R. W., & Gilliland, R. L. 2002, ApJ, 568, 377
Claret, A. 2000, A&A, 363, 1081
Crossfield, I. J. M. 2012, A&A, 545, A97
Crouzet, N., McCullough, P. R., Deming, D., & Madhusudhan, N. 2014, ApJ, 795, 166
Dawson, R. I., & Fabrycky, D. C. 2010, ApJ, 722, 937
Deming, D., Knutson, H., Agol, E., et al. 2011, ApJ, 726, 95
Deming, D., Seager, S., Richardson, L. J., & Harrington, J. 2005, Natur, 434, 740
Deming, D., Wilkins, A., McCullough, P., et al. 2013, ApJ, 774, 95
Demory, B.-O., Gillon, M., Deming, D., et al. 2011, A&A, 533, A114
Demory, B.-O., Gillon, M., Madhusudhan, N., & Queloz, D. 2016, MNRAS, 455, 2018
Demory, B.-O., Gillon, M., Seager, S., et al. 2012, ApJL, 751, L28
Dragomir, D., Matthews, J. M., Winn, J. N., & Rowe, J. F. 2014, in Proc. IAU Symp. 293, Formation, Detection, and Characterization of Extrasolar Habitable Planets, ed. N. Haghighipour (Cambridge: Cambridge Univ. Press), 52
Dressing, C. D., & Charbonneau, D. 2013, ApJ, 767, 95
Fischer, D. A., Marcy, G. W., Butler, R. P., et al. 2008, ApJ, 675, 790
Forget, F., & Leconte, J. 2014, RSPTA, 372, 30084
Fraine, J., Deming, D., Benneke, B., et al. 2014, Natur, 513, 526
Fressin, F., Torres, G., Charbonneau, D., et al. 2013, ApJ, 766, 81
Grasset, O., Schneider, J., & Sotin, C. 2009, ApJ, 693, 722
Gueymard, C. 2004, SoEn, 76, 423
Harris, G. J., Polyansky, O. L., & Tennyson, J. 2002, ApJ, 578, 657
Howard, A. W., Marcy, G. W., Bryson, S. T., et al. 2012, ApJS, 201, 15
Howarth, I. D. 2011, MNRAS, 413, 1515
Hu, R., & Seager, S. 2014, ApJ, 784, 63
Knutson, H. A., Benneke, B., Deming, D., & Homeier, D. 2014a, Natur, 505, 66
Knutson, H. A., Charbonneau, D., Allen, L. E., Burrows, A., & Megeath, S. T. 2008, ApJ, 673, 526
Knutson, H. A., Charbonneau, D., Noyes, R. W., Brown, T. M., & Gilliland, R. L. 2007, ApJ, 655, 564
Knutson, H. A., Dragomir, D., Kreidberg, L., et al. 2014b, ApJ, 794, 155
Kreidberg, L., Bean, J. L., Désert, J.-M., et al. 2014a, ApJL, 793, L27
Kreidberg, L., Bean, J. L., Désert, J.-M., et al. 2014b, Natur, 505, 69
Kreidberg, L., Line, M. R., Bean, J. L., et al. 2015, ApJ, submitted (arXiv:1504.05586)
Kuntschner, H., Bushouse, H., Kümmel, M., & Walsh, J. R. 2009, WFC3 SMOV Proposal 11552: Calibration of the G141 grism, WFC3 Instrum. Sci. Rep. 2009-17 (Garching: ST-ECF)
Kurucz, R. L. 1970, SAOSR, 309, 01
Marcy, G. W., Butler, R. P., Fischer, D. A., et al. 2002, ApJ, 581, 1375
Mayor, M., Marmier, M., Lovis, C., et al. 2011, A&A, submitted (arXiv:1109.2497)
McArthur, B. E., Endl, M., Cochran, W. D., et al. 2004, ApJL, 614, L81
McCullough, P., & MacKenty, J. 2012, Considerations for using Spatial Scans with WFC3, WFC3 Instrum. Sci. Rep. 2012-8 (Baltimore, MD: STScI)
McCullough, P. R., Crouzet, N., Deming, D., & Madhusudhan, N. 2014, ApJ, 791, 55
Nelson, B. E., Ford, E. B., Wright, J. T., et al. 2014, MNRAS, 441, 442
Redfield, S., Endl, M., Cochran, W. D., & Koesterke, L. 2008, ApJL, 673, L87
Rothman, L. S., Gordon, I. E., Babikov, Y., et al. 2013, JQSRT, 130, 4
Rothman, L. S., Gordon, I. E., Barbe, A., et al. 2009, JQSRT, 110, 533
Rothman, L. S., Gordon, I. E., Barber, R. J., et al. 2010, JQSRT, 111, 2139
Seager, S., & Sasselov, D. D. 2000, ApJ, 537, 916
Segura, A., Krelove, K., Kasting, J. F., et al. 2003, AsBio, 3, 689
Snellen, I. A. G., Albrecht, S., de Mooij, E. J. W., & Le Poole, R. S. 2008, A&A, 487, 357
Snellen, I. A. G., Brandl, B. R., de Kok, R. J., et al. 2014, Natur, 509, 63
Snellen, I. A. G., de Kok, R. J., de Mooij, E. J. W., & Albrecht, S. 2010, Natur, 465, 1049
Sotin, C., Grasset, O., & Mocquet, A. 2007, Icar, 191, 337
Stevenson, D. J. 2013, in Gas and Ice Giant Interiors, ed. T. D. Oswalt, L. M. French, & P. Kalas (Dordrecht: Springer), 195
Stevenson, K. B., Désert, J.-M., Line, M. R., et al. 2014, Sci, 346, 838
Swain, M., Deroo, P., Tinetti, G., et al. 2013, Icar, 225, 432
Swain, M. R., Deroo, P., Griffith, C. A., et al. 2010, Natur, 463, 637
Swain, M. R., Tinetti, G., Vasisht, G., et al. 2009a, ApJ, 704, 1616
Swain, M. R., Vasisht, G., & Tinetti, G. 2008, Natur, 452, 329
Swain, M. R., Vasisht, G., Tinetti, G., et al. 2009b, ApJL, 690, L114
Tennyson, J., & Yurchenko, S. N. 2012, MNRAS, 425, 21
Tinetti, G., Deroo, P., Swain, M. R., et al. 2010, ApJL, 712, L139
Tinetti, G., Liang, M.-C., Vidal-Madjar, A., et al. 2007a, ApJL, 654, L99
Tinetti, G., Vidal-Madjar, A., Liang, M.-C., et al. 2007b, Natur, 448, 169
Tsiaras, A., Waldmann, I. P., Rocchetto, M., et al. 2015, ApJ, submitted (arXiv:1511.07796)
Valencia, D., Guillot, T., Parmentier, V., & Freedman, R. S. 2013, ApJ, 775, 10
Valencia, D., Sasselov, D. D., & O'Connell, R. J. 2007, ApJ, 665, 1413
Valenti, J. A., & Fischer, D. A. 2005, ApJS, 159, 141
Varley, R., & Tsiaras, A. 2015, ApJ, submitted (arXiv:1511.09108)
Venot, O., Hébrard, E., Agúndez, M., et al. 2012, A&A, 546, A43
Venot, O., Hébrard, E., Agúndez, M., Decin, L., & Bounaceur, R. 2015, A&A, 577, A33
von Braun, K., Boyajian, T. S., ten Brummelaar, T. A., et al. 2011, ApJ, 740, 49
Waldmann, I. P., Rocchetto, M., Tinetti, G., et al. 2015a, ApJ, 813, 13
Waldmann, I. P., Tinetti, G., Drossart, P., et al. 2012, ApJ, 744, 35
Waldmann, I. P., Tinetti, G., Rocchetto, M., et al. 2015b, ApJ, 802, 107
Wang, H., Warner, S., Oehlschlaeger, M., et al. 2010, CoFl, 157, 1976
Wilkins, A. N., Deming, D., Madhusudhan, N., et al. 2014, ApJ, 783, 113
Winn, J. N., Matthews, J. M., Dawson, R. I., et al. 2011, ApJL, 737, L18
Yurchenko, S. N., Barber, R. J., & Tennyson, J. 2011, MNRAS, 413, 1828
Yurchenko, S. N., & Tennyson, J. 2014, MNRAS, 440, 1649
Zeng, L., & Sasselov, D. 2014, ApJ, 784, 96